Journal of Solid State Chemistry 182 (2009) 2185–2190

Contents lists available at ScienceDirect

Journal of Solid State Chemistry

journal homepage: www.elsevier.com/locate/jssc

Mesoporous mesocrystal $Ce_{1-x}Zr_xO_2$ with enhanced catalytic property for CO conversion

Xiazhang Li [a], Chaoying Ni [b], Feng Chen [c], Xiaowang Lu [c], Zhigang Chen [c,*]

[a] Department of Materials Science and Engineering, Jiangsu University, Zhenjiang 212013, PR China
[b] Department of Materials Science and Engineering, University of Delaware, Newark, DE 19716, USA
[c] Department of Materials Science and Engineering, Jiangsu Polytechnic University, Changzhou 213164, PR China

ARTICLE INFO

Article history:
Received 13 February 2009
Received in revised form
25 April 2009
Accepted 3 May 2009
Available online 9 May 2009

Keywords:
Ceria
Mesoporous
Mesocrystal
Co oxidation

ABSTRACT

Novel mesoporous mesocrystal $Ce_{1-x}Zr_xO_2$ was synthesized using acetate salt as inorganic species and P123 as surfactant. Transmission electron microscopy reveals that the wall framework consists of a single phase based on the face-centered cubic CeO_2 and the nanocrystals are highly oriented with the crystal axis [001] parallel to the pore channel if the Zr^{4+} molar fraction x is 0.3 or less. However, when the Zr^{4+} molar fraction is larger than 0.3, a mixture of cubic and tetragonal phases forms and the preferential crystal orientation disappears as revealed by XRD and Raman measurements. The formation mechanism is ascribed to the oriented attachment following the manner of coherent interface. The single phase solid solution at Zr^{4+} molar fraction 0.3 demonstrates the best catalytic performance for CO conversion due to the unique mesoporous mesocrystal structure with dominant exposure of highly active {200} planes and an enhanced redox property caused by adequate Zr^{4+} incorporation.

1. Introduction

Since the first discovery of the mesoporous silica MCM-41 by Mobil oil researchers in 1992 [1], a variety of mesoporous inorganic oxides with different pore symmetry have been synthesized by using various types of soft templates [2] (cationic, anionic, block copolymer) or hard templates [3] (mesoporous silica, mesoporous carbon). Applications of mesoporous materials now have been widely extended to many areas including catalysis, sensors, control-release, and capacitors. However, due to the limitation of thermal and mechanical stability of the amorphous wall framework of most conventional mesoporous metal oxides [4], there have been considerable efforts in the synthesis of mesostructured materials with crystalline frameworks. There are reports of successful syntheses of crystalline pore walls with randomly oriented nanocrystals [5–8]. To achieve better catalytic activity and enhanced structural and thermal stability, one of the recent progresses has been towards the fabrication of single crystal mesostructures. For instance, Domen group has successfully prepared mesoporous single crystals of mixed Nb and Ta oxides following a soft-template route and found via *in-situ* TEM that the pore was round-shaped with parallel lattice fringes [9–11]. Using a novel solid–liquid route, Zhou group fabricated a series of porous single crystals of Co_3O_4, NiO, CeO_2, CrO_3, and they discovered a uniform crystal orientation of replica nanorods and small bridges [12]. Lou and co-authors report a simple solid-state formation of mesoporous Co_3O_4 nano-needles with a 3D single crystalline framework [13].

To better describe a crystal family whose growth and structure are different from the conventional polycrystal and single crystal, Cölfen and co-authors proposed a new term called mesocrystal [14,15]. A mesocrystal grows via oriented aggregation of individual small crystals such that the overall structural orientation of the resulting larger crystal resembles a single crystal. The driving force for this spontaneous oriented attachment is that the elimination of the pairs of high energy surfaces will lead to a substantial reduction in the surface free energy from the thermodynamic view point [16]. In the recent past, a number of mesocrystal compounds with characteristic morphology have been successfully synthesized [17–21], and more importantly, these mesocrystals are found to showcase unprecedented catalytic and optical properties [22,23].

CeO_2 is an important rare earth oxide and has been widely investigated in the three-way catalysts and solid oxide fuel cell applications; to achieve better catalytic and redox performances, several efforts have been made to fabricate pure mesoporous CeO_2 [24,25] or a mixture of CeO_2 and ZrO_2 [26,27]. However, to the best of the authors' knowledge, the framework of mesoporous CeO_2 or CeO_2–ZrO_2 in most cases consists of randomly oriented polycrystalline, and catalytically active atomic planes are not well

* Corresponding author. Fax: +86 519 86330066.
E-mail addresses: xiazhang@udel.edu (X. Li), czg@ujs.edu.cn (Z. Chen).

0022-4596/$ - see front matter © 2009 Published by Elsevier Inc.
doi:10.1016/j.jssc.2009.05.001

exposed to achieve optimal activity. In previous work, we have fabricated an oriented polycrystalline mesoporous CeO_2 and *in-situ* TEM analysis suggested that the pore framework had excellent thermal stability [28]. Here, we report the synthesis of mesoporous mesocrystal $Ce_{1-x}Zr_xO_2$ with varying Zr^{4+} molar ratios. The structural evolution of the meso-channel wall-frame is investigated. Corresponding physicochemical property and CO conversion in the redox reaction $2CO+O_2 \rightarrow 2CO_2$ are evaluated.

2. Experimental section

2.1. Synthesis

Typically, 1 g of Pluronic P123 (Sigma-Aldrich) was first dissolved in a solution of 15 ml ethanol and 5 ml distilled water, then a total of 0.01 mol of cerium acetate hydrate (Sigma-Aldrich) and zirconium acetate hydrate (Sigma-Aldrich) were added in proportion with Zr^{4+} molar fraction ranging from 0 to 0.8. The mixture was stirred for 2 h to ensure thorough mixing, and subsequently dispersed with a micropipette onto Petri dishes (100 mm in diameter), and was then placed in an oven to form a gel at 40 °C. After 48 h aging, the gel was dried at 80 °C for 24 h. Calcination was carried out by slowly increasing temperature from room temperature to 400 °C (2 °C min^{-1} ramping rate) and heating at 400 °C for 5 h.

2.2. Characterization

TEM characterization was performed using a JEM-2010F field emission transmission electron microscope operating at an accelerating voltage of 200 kV. The samples were supported on carbon–copper grids by dropping ethanol suspensions containing uniformly dispersed oxide powders in ambient environment. The powder X-ray diffraction (XRD) patterns were recorded on Rigaku D/MAX-2500PC diffractometer with Cu target (40 kV, 40 mA) at a scanning rate of 8° min^{-1}. The average grain size D was estimated according to Scherrer equation: $D = 0.89\lambda/\beta\cos\theta$, where θ is the diffraction angle of the main peak and β is the full width at half maximum (FWHM). Vis-Raman spectra were determined on a Renishaw (UK) spectrometer with an Ar ion laser of 514 nm excitation. The N_2 sorption measurement was performed using Micromeritics ASAP 2010 at 77 K, and specific surface area and the pore size distribution were calculated using the Brunauer–Emmett–Telley (BET) and Barrett–Joyner–Halenda (BJH) methods, respectively.

2.3. Catalytic measurement

The catalytic reactions were performed using a continuous-flow fixed-bed microreactor in a temperature-programmed system. In a typical reaction, 150 mg powder was loaded in a stainless tube reactor, and the reactor was heated from room temperature to 800 K at a rate of 2 °C min^{-1}. The total gas flow amounted to 40 ml min^{-1} and the inlet gas composition was 1% CO and 5% O_2 with N_2 as balance. The

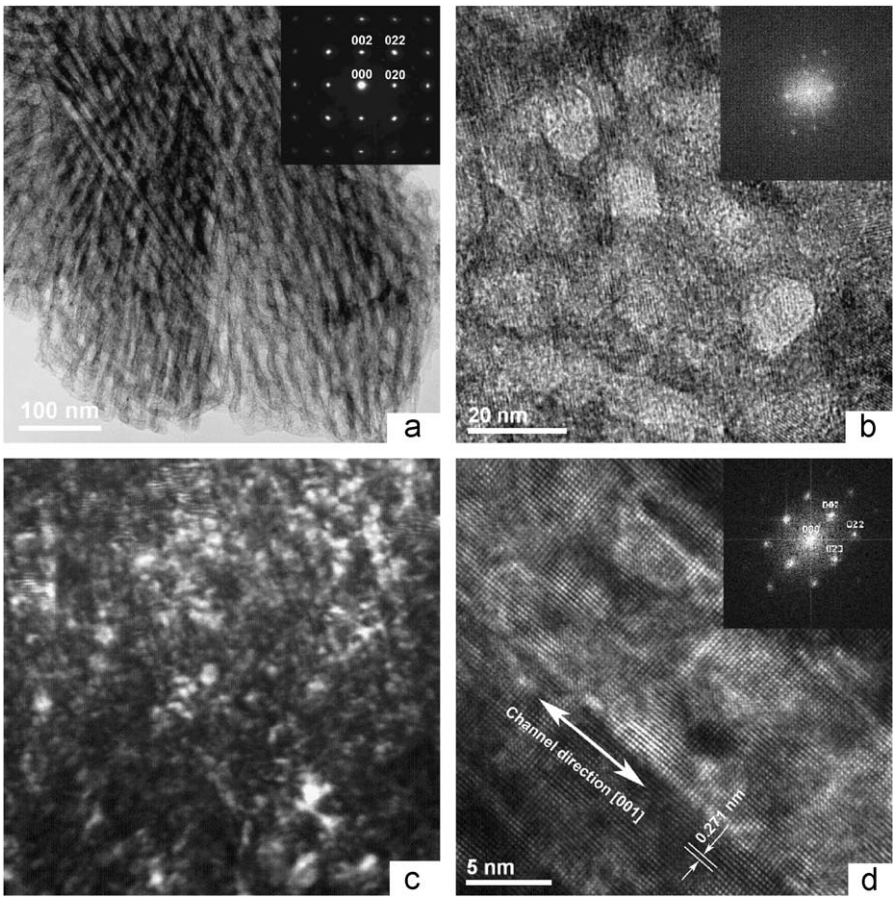

Fig. 1. TEM images of mesoporous mesocrystal CeO_2: (a) [100] orientation and corresponding [100] zone pattern (top-right inset), (b) pore channel in [001] orientation and its [001] FFT pattern (top-right inset), (c) corresponding dark field image of (b), and (d) HRTEM image of a single pore channel and its FFT pattern.

composition of the gas exiting the reactor was monitored online by gas chromatograph (GC 950 system) equipped with a thermal conductivity detector (TCD).

3. Results and discussion

3.1. Evolution of mesoporous mesocrystal structure

Fig. 1a presents the TEM image of arrays of order channel with a diameter of about 10 nm; it is found that the selected area electron diffraction (SAED) pattern from pore channels perpendicular to the electron beam resembles a single crystal [100] zone pattern, as shown in the Fig. 1a inset. Hence, possible mesostructures plausible for this diffraction phenomenon can be either single crystal or mesocrystal. Fig. 1b and c are a pair of bright-field and corresponding dark-field images of an area with pore channels parallel to the beam. The inset FFT pattern in Fig. 1b also looks similar to a single crystal [001] zone pattern. In the dark-field image, however, sporadic bright spots on the dark background indicate the location of reflecting nanocrystals, suggesting the mesoporous structure is in fact a mesocrystal that exhibits an overall single crystal diffraction behavior but is composed of preferentially aligned nanocrystals. A high resolution image of one meso-channel is shown in Fig. 1d. It is noticeable that one set of the lattice fringes is parallel to the meso-channel and the other is perpendicular, and that the reciprocal vectors [020] and [002] in the inset FFT are so oriented as well. The facets of the crystals in the wall framework can also be determined by HRTEM, in which the inter-fringe distance is measured to be 0.271 nm, consistent with the {200} lattice spacing of the cubic phase for ceria [29,30].

For face-centered cubic (fcc) ceria, as illustrated by Wang and Feng [31], the shape of nanocrystal is mainly determined by the ratio (R) between the growth rates along [100] and [111] directions, and crystal aggregation follows the rule of "coherent interface". In this study, the acetate salt and the amphiphilic surfactant are believed to have a synergistic effect on the formation of preferentially oriented polycrystals during the sol–gel process. As the low-order Miller index {200} surface of CeO_2 is less stable, the hydrophilic segments of P123 combined with the acetate group are likely to interact preferentially with {200} atomic planes [32–34], which consequently leads to the maintenance of predominant exposure of {200} facets. In addition, the {200} surfaces have strong dipole–dipole interactions with respect to the van der Waals force, and nanocrystals tend to attach by sharing common crystallographic faces in order to maximize the packing density and lower the surface energy [31,35]. The above interaction between surfactant segments and atomic planes and the strong dipole–dipole force not only promote the mesocrystal formation, but also lead to the aligned pore channels with predominant {200} exposure after the elimination of the polymeric surfactant template by calcination. It should be pointed out that the synergistic effect observed between the acetate salt and the amphiphilic surfactant did not appear to be a mechanism when cerium nitride was used and the resulting structure was noticeably different [23].

Mesoporous structures of $Ce_{1-x}Zr_xO_2$ with varying Zr molar fraction ($x = 0.2$, 0.3, 0.5, 0.8) have also been successfully synthesized by adjusting the input of zirconium acetate hydrate in the reaction system. As can be seen in Fig. 2a and b, the selected

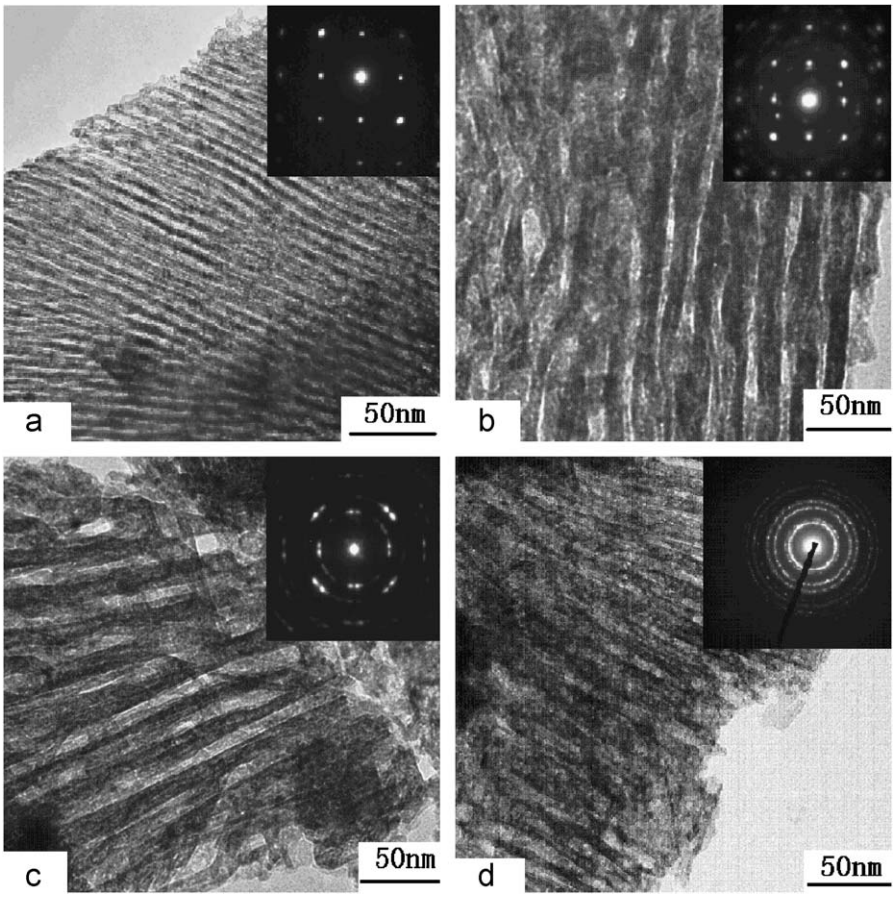

Fig. 2. TEM and corresponding SAED images of mesostructured $Ce_{1-x}Zr_xO_2$: (a) $x = 0.2$, (b) $x = 0.3$, (c) $x = 0.5$, and (d) $x = 0.8$.

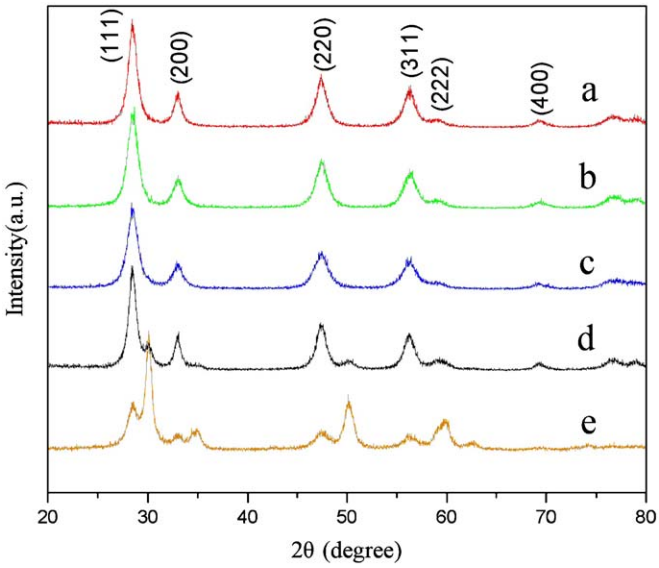

Fig. 3. XRD patterns of mesostructured $Ce_{1-x}Zr_xO_2$: (a) $x = 0$, (b) $x = 0.2$, (c) $x = 0.3$, (d) $x = 0.5$, and (e) $x = 0.8$.

area electron diffraction pattern remains to be similar to a typical single crystal pattern when x is 0.2 or 0.3. However, as the molar fraction rises to 0.5, streaks around reflection dots are easily visible in Fig. 2c. Eventually, typical polycrystal ring patterns are observed when $x = 0.8$ (Fig. 2d). ZrO_2 has the same fluorite lattice as CeO_2. According to an available CeO_2-ZrO_2 phase diagram [36,37], Zr^{4+} can substitute Ce^{4+} to form $Ce_{1-x}Zr_xO_2$ solid solutions over full range of the molar ratio. However, $Ce_{1-x}Zr_xO_2$ can exist in three stable phases, monoclinic (m), tetragonal (t) and cubic (c), and two metastable phases (t', t'') under different conditions [38]. And it would also be thermodynamically plausible to have regions in the phase diagram where more than one of the above phases would coexist at room temperature though the true nature of the phase boundaries is still unclear. In this study, XRD diffraction indicate that meso-crystalline $Ce_{1-x}Zr_xO_2$ has face-centered cubic structure for compositions at $x < 0.5$, as shown in Fig. 3(a)–(c), and the peaks of CeO_2 in XRD slightly shift to the higher degree with increase of x value. Around $x = 0.5$, a second phase indexable as from a tetragonal structure starts to appear in Fig. 3(d), and at $x = 0.8$, this phase dominates in the two phase mixture as shown in Fig. 3(e). The XRD results are also confirmed by Raman spectroscopy. For the sample with molar fraction $x = 0$, 0.2, and 0.3 in Fig. 4, a single peak appears between 461 and 465 cm^{-1}, indicating the F_{2g} mode for cubic CeO_2. When the molar ratio x reaches 0.8, six active modes of $A_{1g}+3E_g+2B_{1g}$ symmetry (Fig. 4e, five located at 113, 266, 313, 463, and 632 cm^{-1} plus one shoulder at ca. 563 cm^{-1}) are observed, confirming a dominant Zr^{4+} rich tetragonal phase mixed with minor cubic phase [33]. It is noteworthy that the F_{2g} band in Raman spectra decreased in intensity greatly but not linearly from (a) to (d), which might be on account of the increasing structural defects in the mesocrystal units with the introduction of Zr content. Above results also suggest that as the Zr^{4+} molar ratio increases, while the phase evolution does not significantly alter the morphology of the mesoporous channels, it does have an effect on the meso-crystallinity. Relatively low Zr^{4+} molar ratio in $Ce_{1-x}Zr_xO_2$ can still maintain a predominant cubic structure to achieve the coherent crystal alignment. When x is higher than 0.3, however, the tetragonal phase co-precipitates with the cubic phase, and the dissimilarity in crystal structures eventually leads to a random orientation of the polycrystals.

Sample porosity was tested by N_2 adsorption–desorption isotherm and by Barrett–Joyner–Halenda pore size distribution analysis for the desorption branch of the isotherm. All the isotherms in Fig. 5 can be categorized as type IV hysteresis loop, characteristic of capillary condensation taking place in mesopores. Typical BJH pore size distribution for sample with $x = 0.3$ shows a relatively narrow pore size distribution between 8 and 12 nm, consistent with the TEM measurement of the channel diameter of around 10 nm. Table 1 summarizes the textural properties of the mesostructured $Ce_{1-x}Zr_xO_2$. The sample with $x = 0.3$ has the largest BET surface area 154 $m^2 g^{-1}$ and the highest pore volume 0.21 $cm^3 g^{-1}$, which is probably attributable to a positive

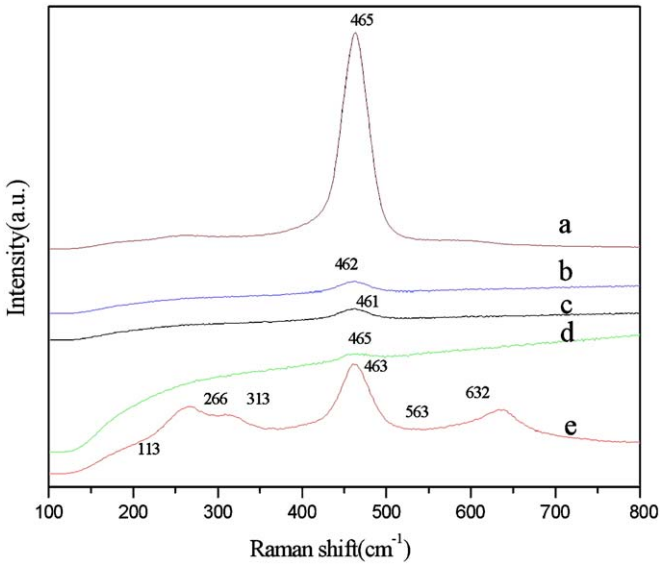

Fig. 4. Vis-Raman spectra of mesostructured $Ce_{1-x}Zr_xO_2$: (a) $x = 0$, (b) $x = 0.2$, (c) $x = 0.3$, (d) $x = 0.5$, and (e) $x = 0.8$.

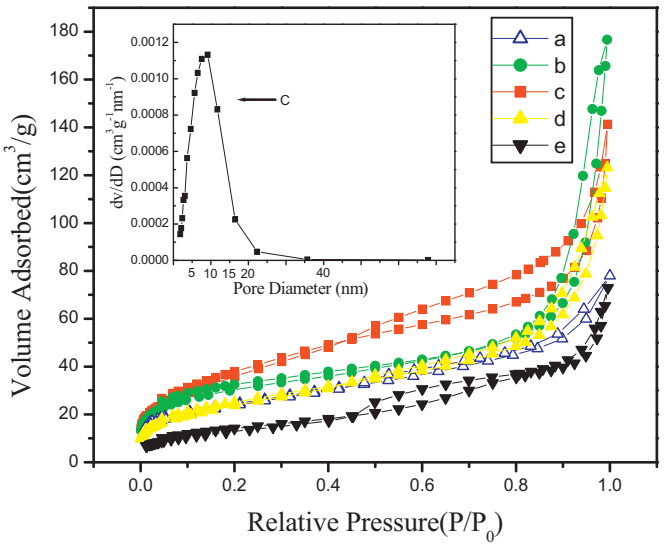

Fig. 5. Nitrogen adsorption–desorption isotherms of mesostructured $Ce_{1-x}Zr_xO_2$: (a) $x = 0$, (b) $x = 0.2$, (c) $x = 0.3$, (d) $x = 0.5$, and (e) $x = 0.8$; inset: corresponding pore size distribution of (c) deduced from the desorption branches.

Table 1
Summary of the textual properties of mesostructured $Ce_{1-x}Zr_xO_2$.

Sample (x ratio)	Crystalline size (nm)	BET surface area ($m^2 g^{-1}$)	Pore volume ($cm^3 g^{-1}$)
0	5.5	139	0.16
0.2	5.3	135	0.18
0.3	4.9	154	0.21
0.5	4.7	115	0.14
0.8	4.3	98	0.11

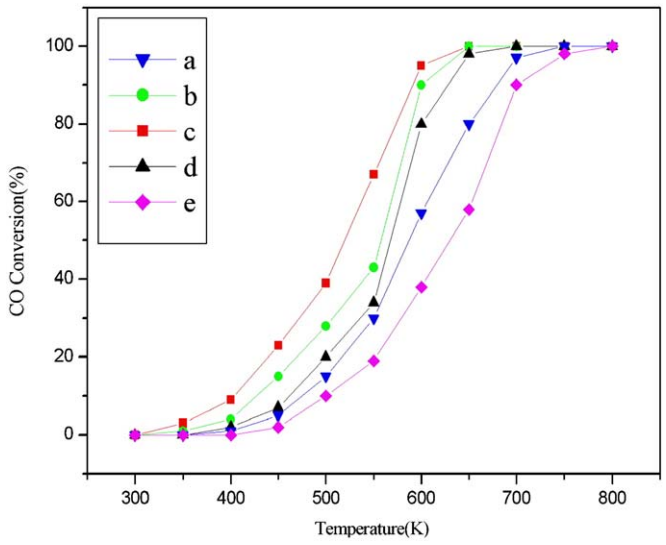

Fig. 6. Percentage of CO conversion for $CO+O_2$ reaction over mesostructured $Ce_{1-x}Zr_xO_2$: (a) $x = 0$, (b) $x = 0.2$, (c) $x = 0.3$, (d) $x = 0.5$, and (e) $x = 0.8$.

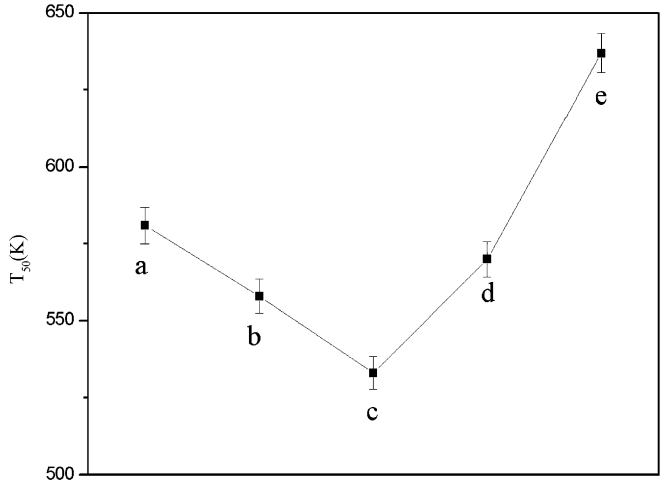

Fig. 7. T_{50} of mesostructured $Ce_{1-x}Zr_xO_2$: (a) $x = 0$, (b) $x = 0.2$, (c) $x = 0.3$, (d) $x = 0.5$, and (e) $x = 0.8$.

physicochemical contribution from adding Zr dopant to an optimal amount with no appreciable crystal structural and morphological changes.

3.2. CO oxidation property

The conversion profiles of CO versus temperature are shown in Fig. 6. Prior to all catalytic experiments, samples were pre-treated *in-situ* in reaction conditions identical to those of the second runs used for actual data collection. The temperatures for 50% conversion of carbon monoxide (T_{50}) are shown in Fig. 7. It is noted that the T_{50} of the pure mesoporous mesocrystal CeO_2 ($T_{50} = 581$ K) in this study is lower than what was reported by Lundberg and co-workers ($T_{50} = 608$ K), where the BET surface area was similar [21]. This can be due to the dominant exposure of {200} atomic planes in the mesoporous mesocrystal structure and the {200} planes are more likely to accommodate reactions with CO since less energy is required to form an anion vacancy with new oxygen on these surfaces [39]. Therefore, the favorable crystal surface is good for the catalytic reaction. Increasing the Zr^{4+} content further decreases the T_{50} until the lowest T_{50} is achieved at 533 K for samples with Zr^{4+} molar fraction of 0.3. It could be due to the fact that the introduction of Zr^{4+} may give rise to more oxygen vacancies without decreasing the active planes; also the high surface area at this optimal fraction was believed to contribute to the enhanced catalytic performance. Afterwards, the physicochemical enhancement from Zr^{4+} doping is offset by the formation of the tetragonal phase and the structural misalignment. Significant increase of T_{50} is observed as high as 637 K for the sample with Zr^{4+} molar fraction of 0.8.

There are reports that the addition of ZrO_2 to CeO_2 host can improve thermal stability and catalytic property [40,41]. The results in this study suggest that the doping effect is not linear. The favorable enhancement can be further exploited by fabricating porous mesocrystals with the preferential alignment of mesochannels. However, over-doping Zr^{4+} into CeO_2 results in the formation of mixed phases and the interruption to mesocrystal coherency, and the resulting catalyst has lower surface area and fewer active crystal faces. It should be pointed out that to fully understand the mechanism, further research particularly combined with computer modeling is necessary.

4. Conclusions

In summary, mesoporous mesocrystal $Ce_{1-x}Zr_xO_2$ is synthesized by choosing acetate salt as inorganic species and P123 as surfactant. The pore channels are found to be about 10 nm in diameter. More interestingly, the channel wall framework consists of highly oriented $Ce_{1-x}Zr_xO_2$ crystals with the crystal axis [001] parallel to the pore channel and the {200} planes dominating the channel surface. It is believed that the hydrophilic segments of P123 and the acetate group act synergistically to promote the formation of pore channel surfaces with dominant {200} planes, and the strong dipole–dipole interactions following the manner of coherent interface assist the alignment of the crystal orientation to form mesocrystals. Such mesocrystal preferential alignment is maintained when the Zr^{4+} molar fraction in $Ce_{1-x}Zr_xO_2$ is less than 0.3. However, more doping leads to forming a mixture of cubic and tetragonal phases and losing the preferential crystal orientation. The physicochemical contribution from Zr^{4+} doping and the structural evolution result in an optimal structure at $x = 0.3$ for CO conversion. Given the versatility of the synthetic approach, further research is warranted in the exploration of a series of ceria-based mesoporous mesocrystals with various dopants.

Acknowledgments

This work was financially supported by the National Science Foundation of China (NSFC20771047), Provincial Science Foundation of Jiangsu (BK2008541), High-tech Project of Jiangsu (BE2008033), and Jiangsu University Innovation Grant (1293000425).

References

[1] C.T. Kresge, M.E. Leonowicz, J. Roth, J.C. Vartuli, J.S. Beck, Nature 359 (1992) 710–712.
[2] F. Schűth, Chem. Mater. 13 (2001) 3184–3195.
[3] M. Tiemann, Chem. Mater. 20 (2008) 961–971.
[4] J.N. Kondo, K. Domen, Chem. Mater. 20 (2008) 835–847.
[5] H.R. Chen, J.L. Gu, J.L. Shi, Z.C. Liu, J.H. Gao, M.L. Ruan, D.S. Yan, Adv. Mater. 17 (2005) 2010–2014.
[6] H.P. Zhou, Y.W. Zhang, R. Si, L.S. Zhang, W.G. Song, C.H. Yan, J. Phys. Chem. C 112 (2008) 20366–20374.
[7] J.N. Kondo, K. Domen, Chem. Mater. 20 (2008) 835–847.
[8] Y. Wan, Y.F. Shi, D.Y. Zhao, Chem. Mater. 20 (2008) 932–945.
[9] B. Lee, D. Lu, J.N. Kondo, K. Domen, Chem. Commun. (2001) 2118–2119.
[10] B. Lee, T. Yamashita, D. Lu, J.N. Kondo, K. Domen, Chem. Mater. 14 (2002) 867–875.
[11] D. Lu, T. Katou, M. Uchida, J.N. Kondo, K. Domen, Chem. Mater. 17 (2005) 632–637.
[12] W.B. Yue, W.Z. Zhou, Chem. Mater. 19 (2007) 2359–2363.
[13] X.W. Lou, D. Deng, J.Y. Lee, L.A. Archer, J. Mater. Chem. 18 (2008) 4397–4401.
[14] H. Cölfen, M. Antonietti, Angew. Chem. Int. Ed. 44 (2005) 5576–5591.
[15] T. Wang, H.C. Cölfen, M. Antonietti, Chem. Eur. J. 12 (2006) 5722–5730.
[16] Q. Zhang, S.J. Liu, S.H. Yu, J. Mater. Chem. 19 (2009) 191–207.
[17] J.S. Fang, H.J. You, P. Kong, Y. Yi, X.P. Song, B.J. Ding, Cryst. Growth. Des. 7 (2007) 864–867.
[18] J.X. Fang, X.N. Ma, H.H. Cai, X.P. Song, B.J. Ding, Nanotechnology 17 (2006) 5841–5845.
[19] J.X. Fang, B.J. Ding, X.P. Song, Cryst. Growth. Des. 8 (2008) 3612–3616.
[20] J.X. Fang, B.J. Ding, X.P. Song, Y. Han, Appl. Phys. Lett. 92 (2008) 173120–173123.
[21] J.X. Fang, B.J. Ding, X.P. Song, Appl. Phys. Lett. 91 (2007) 083108–083110.
[22] M.S. Mo, S.H. Lim, Y.W. Mai, R.K. Zheng, S.P. Ringer, Adv. Mater. 20 (2008) 339–342.
[23] Z.H. Li, A. Geβner, J.P. Richters, J. Kalden, T. Voss, C. Kűbel, A. Taubert, Adv. Mater. 20 (2008) 1279–1285.
[24] W.H. Shen, X.P. Dong, Y.F. Zhu, H.R. Chen, J.L. Shi, Micropor. Mesopor. Mater. 85 (2005) 157–162.
[25] P.F. Ji, J.L. Zhang, F. Chen, M. Anpo, J. Phys. Chem. C 112 (2008) 17809–17813.
[26] T. Brezesinski, M. Antonietti, M. Groenewolt, N. Pinna, B. Smarsly, New. J. Chem. 29 (2005) 237–242.
[27] R. Si, Y.W. Zhang, C.X. Xiao, S.J. Li, B.X. Lin, Y. Kou, C.H. Yan, Phys. Chem. Chem. Phys. 6 (2004) 1056–1063.
[28] C.Y. Ni, X.Z. Li, Z.G. Chen, H. Li, X.Q. Jia, I. Shah, J.Q. Xiao, Micropor. Mesopor. Mater. 115 (2008) 247–252.
[29] X.D. Feng, D.C. Sayle, Z.L. Wang, M.S. Paras, B. Santora, A.C. Sutorik, T. Sayle, Y. Yang, Y. Ding, X.D. Wang, Y.S. Her, Science 312 (2006) 1504–1508.
[30] K. Kaneko, K. Inoke, B. Freitag, A.B. Hungria, P.A. Midgley, T.W. Hansen, J. Zhang, S. Ohara, T. Adschiri, Nano Lett. 7 (2007) 421–425.
[31] Z.L. Wang, X.D. Feng, J. Phys. Chem. B 107 (2003) 13563–13566.
[32] C.Y. Ni, P.A. Hassan, E.W. Kaler, Langmuir 21 (2005) 3334–3337.
[33] Q. Yuan, Q. Liu, W.G. Song, W. Feng, W.L. Pu, L.D. Sun, Y.W. Zhang, C.H. Yan, J. Am. Chem. Soc. 129 (2007) 6698–6699.
[34] J. Zhang, S. Ohara, M. Umetsu, T. Naka, Y. Hatakeyama, T. Adschiri, Adv. Mater. 19 (2007) 203–206.
[35] M. Mo, J.C. Yu, L.Z. Zhang, S.K.A. Li, Adv. Mater. 17 (2005) 756–760.
[36] M. Yashima, K. Morimoto, N. Ishizawa, M. Yoshimura, J. Am. Ceram. Soc. 76 (1993) 1745–1750.
[37] M. Yashima, K. Morimoto, N. Ishizawa, M. Yoshimura, J. Am. Ceram. Soc. 76 (1993) 2865–2868.
[38] X. Liang, X. Wang, Y. Zhuang, B. Xu, S. Kuang, Y.D. Li, J. Am. Chem. Soc. 130 (2008) 2736–2737.
[39] C.S. Pan, D.S. Zhang, L.Y. Shi, J. Solid State Chem. 181 (2008) 1298–1306.
[40] M.L. Teng, L.T. Luo, X.M. Yang, Micropor. Mesopor. Mater. 119 (2009) 158–164.
[41] P. Singh, M.S. Hegde, J. Solid State Chem. 181 (2008) 3248–3256.